The Astrophysical Journal, 668:316–330, 2007 October 10

TOTAL TO SELECTIVE EXTINCTION IN THE DARK GLOBULE CB 107

L. Campeggio, F. Strafella,[1] B. Maiolo, and D. Elia
Dipartimento di Fisica, Università del Salento, I-73100 Lecce, Italy; campeggio@le.infn.it, strafella@le.infn.it, maiolo@le.infn.it, eliad@le.infn.it

and

S. Aiello
Dipartimento di Astronomia e Scienza dello Spazio, Università di Firenze, I-50125 Firenze, Italy; aiello@unifi.it
Received 2007 March 28; accepted 2007 June 18

ABSTRACT

We discuss optical (B, V, and I) and near-infrared (J, H, and K_s) imaging observations of the small dark cloud CB 107. The cloud is projected against a rich stellar background, making it possible to detect ~3900 stars in all six photometric bands. After an accurate choice of a reference region, we obtained the color excess $E_{\lambda-V}$ maps and derived the distribution of the total to selective extinction R_V across the cloud by adopting three different techniques. The R_V map obtained closely follows the optical shape of CB 107 with the value $R_V \simeq 3.1$, typical of the diffuse interstellar medium, corresponding to the optical limit of the globule. Larger values up to $R_V \sim 5$ are found in the innermost regions, indicating an increase in the dust grain mean size. On the basis of our results, the three methods adopted have been found to be almost equivalent. We also estimated the R_V values along the lines of sight of individual stars that, considered in a given spatial box, have been used to obtain both average value and dispersion, as a function of the position. A scatter plot of these two quantities shows that the dispersion σ_{R_V} increases with R_V similarly to the correlation between extinction dispersion σ_{A_V} and A_V already known in the literature. Finally, we discuss the R_V versus A_V scatter plot on the basis of a simple model that helps us to give a plausible physical interpretation of this correlation.

Subject headings: dust, extinction — ISM: globules — ISM: individual (CB 107) — ISM: structure

1. INTRODUCTION

The extinction of the stellar light due to the dusty interstellar medium (ISM) is wavelength dependent, decreasing with increasing wavelength. A thorough study of this effect is clearly important because the spectral behavior of the extinction, being related to the optical properties of the IS dust along the line of sight, can provide information about composition, size distribution, and morphology of the dust grains. The dependence of the extinction on wavelength is usually quantified by the extinction curve, an observable that, in general, depends on the line of sight. An accurate knowledge of this curve is clearly important not only for investigating the nature of the IS dust, but also to correct the observational data for the extinction effect.

The observed extinction curves, accurately obtained in different lines of sight, can be well described by a one-parameter family of fitting functions, as originally proposed by Cardelli et al. (1989, hereafter CCM). The parameter characterizing the shape of a particular extinction curve is the total to selective extinction ratio R_V that is defined by

$$\frac{A_\lambda}{E_{B-V}} = \frac{E_{\lambda-V}}{E_{B-V}} + R_V, \tag{1}$$

where A_λ is the extinction in magnitudes at a given wavelength λ, and $E_{\lambda_1-\lambda_2} = A_{\lambda_1} - A_{\lambda_2}$ is the color excess between the wavelengths λ_1 and λ_2.

An important point is that the steepness of the extinction curve in the optical region depends on the grain size distribution and, from an observational point of view, gives rise to different values of the parameter R_V. Because of this, its value is usually interpreted as a signature of the mean size of the dust grains in a given line of sight. By considering now that the extinction decreases with the wavelength until it becomes asymptotically negligible, we find that R_V can be also related to the normalized excesses by the limit

$$R_V = -\lim_{\lambda\to\infty} \frac{E_{\lambda-V}}{E_{B-V}}, \tag{2}$$

an expression suggesting that R_V can be evaluated by extrapolating the observed extinction curve toward the long wavelengths.

It is customary to use the observed color excesses to define an average Galactic extinction curve corresponding to the case $R_V \simeq 3.1$, a value which is adopted as a reference because it is more frequently found in the diffuse ISM (see, e.g., Whittet & van Breda 1980; Rieke & Lebofsky 1985; CCM). However, values as small as $R_V \sim 1.7$ (e.g., Szomoru & Guhathakurta 1999) for diffuse interstellar dust clouds, and as large as $R_V \sim 5$–7 in more dense environments, such as molecular clouds, have been reported in the literature (see, e.g., Vrba et al. 1981; Strafella et al. 2001; Ducati et al. 2003; Kandori et al. 2003; Balázs et al. 2004).

Many theoretical studies also suggest that the larger R_V values, often found in dense environments, can be due to significant changes in dust properties (e.g., Mathis 1990; Whittet et al. 2001) induced by grain growth processes which are activated in regions of higher density. In fact, when the mean grain size approaches the optical wavelengths, the extinctions in the B and V bands tend to be similar, producing a corresponding increase in R_V. In terms of size distribution, we can assume that the standard value $R_V = 3.1$, characteristic of the diffuse IS regions, separates the cases corresponding to overabundance ($R_V < 3.1$) and underabundance ($R_V > 3.1$) of small grains.

It is then clear that the shape of the extinction curve, parameterized by the value of the total to selective extinction R_V, gives important information on the mean size of the IS grains. Although

[1] Also at I.F.S.I.-INAF, Roma, Italy.

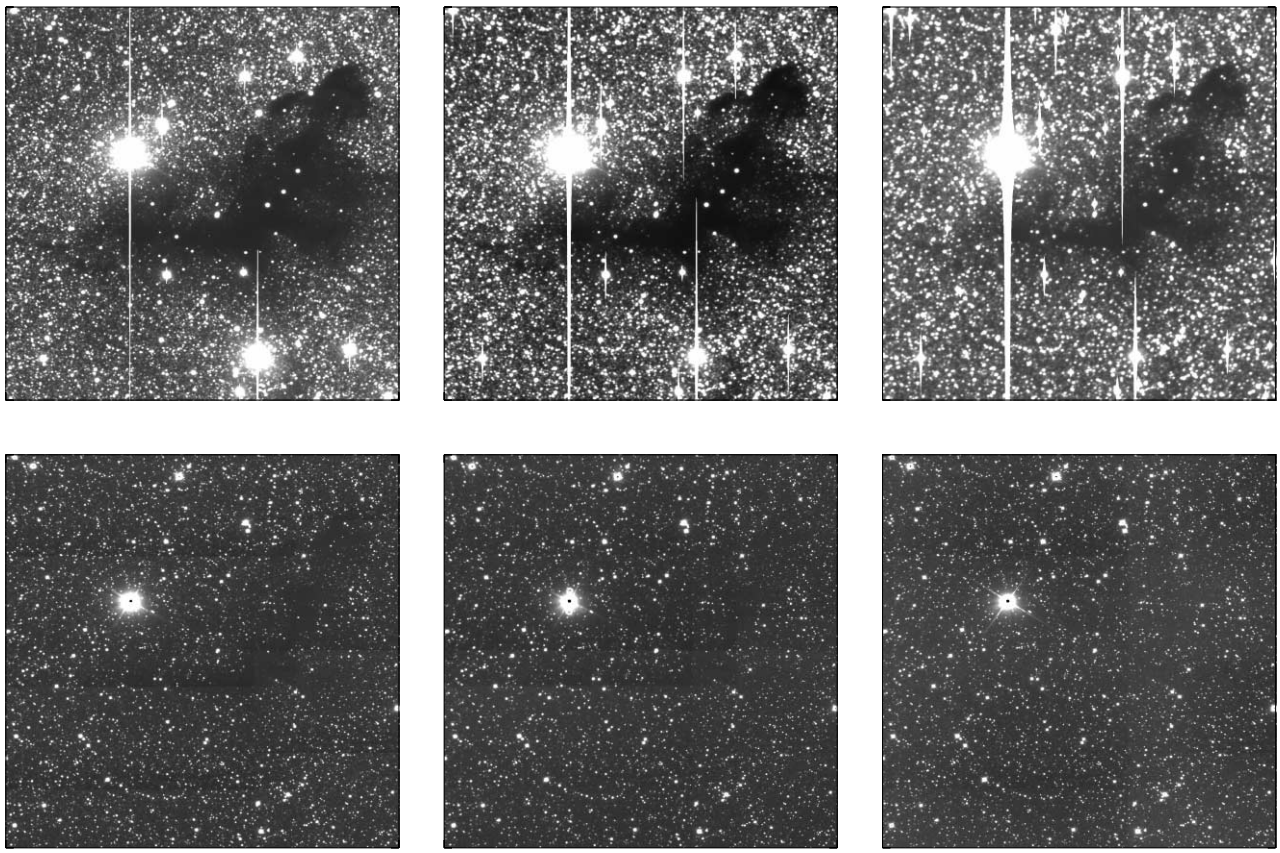

FIG. 1.— Final images of the dark globule CB 107. In the top panels, from left to right, the *B*-, *V*-, and *I*-band images are shown, while in the bottom panels the *J*-, *H*-, and K_s-band images are presented. The central position corresponds to $\alpha(\mathrm{J2000.0}) = 18^{\mathrm{h}}02^{\mathrm{m}}59^{\mathrm{s}}$, $\delta(\mathrm{J2000.0}) = -27^{\circ}50'34''$. The field of view is $6.9' \times 7.5'$, and the orientation is north to the left, west toward the top. Note the wavelength dependence of the dark region.

a considerable number of observational studies have evaluated R_V along lines of sight crossing different interstellar regions, only in a very few cases has the variation of R_V been studied within a given cloud.

In this paper, we use *B*, *V*, *I*, *J*, *H*, and K_s photometry to obtain the color excesses of the background stars and then the corresponding extinction curves $E_{\lambda-V}/E_{B-V}$ in an attempt to study the variation of the R_V parameter across the dark cloud CB 107, along as many lines of sight as possible. In § 2, we briefly describe the acquisition, reduction, and analysis of the observational data, while in § 3 we derive the mean color excesses $E_{\lambda-V}$, which were used to determine the spatial distribution of R_V across CB 107. In § 4, we discuss different methods to determine R_V and consider their uncertainties. In § 5, the observations are also discussed in the light of a simple model, and finally in § 6 we give a summary of the main results and conclusions.

2. OBSERVATIONS AND DATA ANALYSIS

CB 107 is a small molecular cloud located at an estimated distance $d \sim 180$ pc (Launhardt & Henning 1997) toward the Galactic center ($l = 2.8528^{\circ}$, $b = -2.7538^{\circ}$), and thus projected on a rich stellar background. Because the present analysis is based on observational material already discussed in previous papers (Strafella et al. 2001; Campeggio et al. 2004), here we only give a brief account of the data processing relevant to this study.

The observations were carried out at the ESO-NTT telescope with the EMMI (*B*, *V*, and *I* photometric bands) and SOFI (*J*, *H*, and K_s) imagers. Because CB 107 is approximately $5'$ in angular extension, a mosaicking technique was used to fully cover the object and the neighboring stellar field. This procedure was combined with a dithering technique to reject artifacts and increase the signal-to-noise ratio. The standard stars, observed to calibrate our photometry, were selected from the lists of Landolt (1992) and Persson et al. (1998) for the optical and near-IR spectral range, respectively. As usual, ancillary bias, dark, and flat-field frames were also acquired for the purpose of correcting the images for systematics.

After reducing the raw data (following the procedures usually applied to CCD imaging; see, e.g., Strafella et al. 2001; Campeggio et al. 2004), each dithered frame was registered on a common spatial reference by using affine geometric transformations. This procedure gives a subpixel matching among stellar centroids in different frames, thus allowing the merging of the different observations in a final image.

Once these images were obtained, one for each filter, they were in turn registered on a common reference in order to exploit the spatial correspondence for deriving the stellar colors. In doing this, we also considered the different scales and fields of view of the focal plane optical and near-IR imagers. The final images obtained for the dark globule CB 107 are shown in Figure 1.

At first glance these images show that the opacity of the cloud decreases from the optical to the near-IR spectral range, where the stellar background appears more and more uniform until, in the K_s band, we perceive what is practically an absence of extinction. Note that, because the stellar field is quite crowded, it was difficult to select, by automatic procedures, common stars for registering in the same reference both the optical and the near-IR images. This step was accomplished by recognizing, by eye, common stars in the *I* and *J* images that were at the interface between the two spectral regions. These pivotal stars were chosen to cover

the whole image uniformly, and their relative distances were subsequently checked for consistency by means of a triangulation technique (Valdes et al. 1995).

The images were analyzed for photometry by using the DAOPHOT package (Stetson 1987), which involves a star-finding algorithm and a first estimate of the instrumental magnitudes. The final photometry was carried out by means of a point-spread function (PSF) fitting procedure. As a result we obtained, for each filter, a list of centroids and magnitudes from which we discarded the "bad" detections, i.e., those with a photometric uncertainty in the PSF fit larger than $\delta m = 0.1$ mag.

Finally, the instrumental magnitudes were converted in a standard photometric system by using the observed standard stars. The stellar colors were then derived by positional coincidence of the photometry obtained for the six images. In this way, the colors $\lambda - V$, with λ running on the filter used, were obtained for $\sim$3900 stars detected in all six bands, with a photometric error in color $\delta(\lambda - V) < 0.13$ mag. Note that 97% of the stars have $\delta(\lambda - V) < 0.1$ mag.

3. COLOR EXCESSES

The color excess of a reddened star is defined as

$$E_{\lambda-V} = (\lambda - V)_{\rm red} - (\lambda - V)_{\rm int}, \quad (3)$$

where $(\lambda - V)_{\rm red}$ and $(\lambda - V)_{\rm int}$ are the observed (reddened) and intrinsic colors, respectively. Because the intrinsic colors are given once the spectral type is known, a difficulty arises due to the lack of prior information on the spectral type of the detected stars.

It is customary to circumvent this problem statistically, by considering the color distribution instead of the single stellar color. This means that to determine the color distribution we shall use all the stars in a given spatial box, thus sacrificing the spatial resolution in favor of obtaining an averaged color excess. An important assumption underlying this approach is that the stellar population is homogeneous across the observed field, so that any change in the observed color distribution can be associated with the intervening IS medium. Thanks to the large number of stars detected in the investigated field, this is the approach we shall use to determine the color excess, and then to investigate the spatial variations of R_V in CB 107.

By adopting an appropriate spatial grid, it is possible to obtain a map of the color excesses, under the assumption that the mean intrinsic colors of the stellar population in a generic spatial box are well represented by the mean stellar colors in a reference, unreddened field, namely:

$$\langle \lambda - V \rangle_{\rm int} = \langle \lambda - V \rangle_{\rm ref}. \quad (4)$$

This method, often referred to as the NICE[2] method, was developed by Lada et al. (1994) to exploit the possibilities offered by near-IR imaging to obtain the color excesses of the background stars, and to deeply probe the obscured IS regions. In the same line Arce & Goodman (1999), by using an optical version (in V and R bands) of this method, showed that the extinctions determined in different lines of sight for the Taurus complex are consistent with those derived by other methods, such as the canonical method based on the color excess of stars with known spectral type, the method using *IRAS* 60 and 100 μm flux densities, and finally the stellar counts method. More recently, Kandori et al. (2003) applied a similar method to the optical images (B, V, R, and I bands) to derive the color excess distribution in the dark cloud L1251. These authors, using the color excesses and the empirical relation between R_V and A_λ/A_V (CCM), were able to derive the distribution of R_V across the observed cloud. In the same line, we shall assume in the present work that the mean intrinsic stellar colors $\lambda - V$ are well represented, in the whole investigated field, by the mean stellar colors derived in a reference, unreddened region.

To establish an appropriate reference region as free as possible from extinction, we divided our images with a spatial grid, obtaining in each position the $\lambda - V$ color histograms with a square box of size $L \sim 60''$. This size was a trade-off between the need for a statistically significant number of stars and the highest possible spatial resolution. In Figure 2, we present two panels showing the resulting partition of the field superimposed on the J image (*top*) and the corresponding histograms obtained in the $B - V$ color (*bottom*).

It is apparent that the number of detected stars, reported in each box of Figure 2 (*bottom*), decreases from the outer to the inner regions of the globule, being a maximum in box [1, 5] (119 stars) and a minimum in box [5, 4] (16 stars). To verify the background homogeneity, we considered 10 boxes, marked in the top panel of Figure 2, with the lower mean colors $\lambda - V$, which are reported in Table 1, along with their 1 σ dispersion. Despite the different locations of the corresponding boxes, these color values are quite similar; therefore, we decided to use their mean value, reported in the last row of the table, as representative of the reference region. This choice is also supported by the low dispersion of the mean colors of Table 1, which justifies the assumption of homogeneity for the background stellar population across the observed field.

Since it is already known that the surroundings of CB 107 are veiled by a large-scale extinction (Strafella et al. 2001), the reference regions cannot be considered as completely unextinguished; to evaluate this veiling we used the two-color $B - V$ versus $V - I$ diagram. This allowed us to derive the color excesses E_{B-V} and E_{V-I} for a subset of stars (see Strafella et al. 2001 for details). The average values obtained in each marked box for the E_{B-V} excess are reported in the last column of Table 1, and their similarity suggests that we can safely consider a uniform extinction to be veiling this field.

Given the presence of the veiling extinction, the color excesses derived by comparing the stellar colors with those obtained in the reference region are consequently underestimated. To account for this, we assumed that the dust effects in the lines of sight outside the globule are well represented by a standard extinction law so that, once a color excess is measured for the reference region, the whole set of $E_{\lambda-V}$ color excesses can be derived and used to compensate for the global effect of the veiling. In this way, we recovered the intrinsic mean stellar colors in the reference region as

$$\langle \lambda - V \rangle_{\rm int} = \langle \lambda - V \rangle_{\rm ref} - \langle E_{\lambda-V} \rangle_{\rm ref}. \quad (5)$$

Thus, to obtain the corrected color excesses in our photometric bands, we used the Martin & Whittet (1990) average extinction curve for diffuse clouds, which has been interpolated in the near-IR with a power law

$$\frac{E_{\lambda-V}}{E_{B-V}} = \frac{A_\lambda}{E_{B-V}} - R_V = \epsilon \lambda^{-\beta} - R_V, \quad (6)$$

where $\epsilon = 1.19$, $\beta = 1.84$, and $R_V = 3.05$ are constants appropriate for the diffuse IS medium (see Whittet 2003).

By using this interpolation, we derived the normalized color excesses for the ESO filters we used. These values were then multiplied

[2] See also Lombardi & Alves (2001) for an extension to multiband studies.

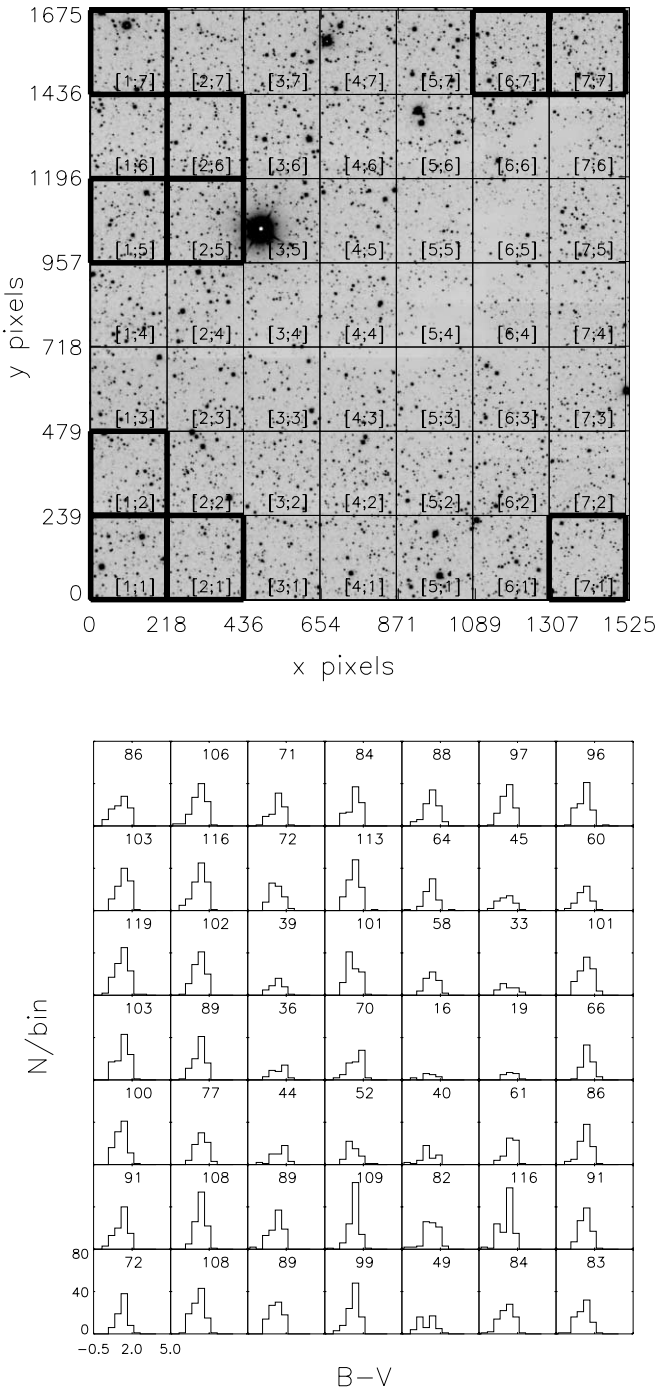

FIG. 2.—Adopted 7×7 grid box superimposed on the image in the J band (*top*). The box size is $L \sim 60''$ and the reference boxes (see text) are marked. The box [1, 1] is in the lower left corner, while the box [7, 7] is in the upper right. In the bottom panel, the $B - V$ stellar color histogram is shown for each box with the number of involved stars indicated. The axes in each box are the same as those shown in the lower left corner.

by the mean $\langle E_{B-V} \rangle$ of the reference region to obtain the whole set of color excesses in this region, namely, $\langle E_{B-V} \rangle = 0.36$, $\langle E_{V-I} \rangle = 0.45$, $\langle E_{V-J} \rangle = 0.81$, $\langle E_{V-H} \rangle = 0.93$, and $\langle E_{V-K} \rangle = 0.99$, respectively. Taking this into account, we obtained the color excess maps by scanning our images with a square counting box of size $L \sim 60''$ in steps of half this size, to obtain a Nyquist spatial sampling. For each box, the excesses were computed as a difference between the mean stellar colors and the intrinsic colors previously determined.

Note that, although the median is a more robust estimator, particularly in regions of low stellar surface density, where foreground stars could strongly bias the mean colors (Lada et al. 1994; Cambrésy 1999), we used the mean colors because the contribution of foreground stars toward CB 107 has been estimated to be negligible, even in the most extinguished regions (Campeggio et al. 2004).

3.1. *Uncertainties*

In evaluating the uncertainty of the color excesses, we considered two main sources: one that referred to the colors determined for the reference region, and the other related to the photometric errors. Note that, while in the first case the same error applies to all the objects, the photometric errors are different from star to star. Thus, following Arce & Goodman (1999) and Kandori et al. (2003), the uncertainty in the average color for a given spatial box is

$$\Delta(\lambda - V) = \sqrt{[\sigma(\lambda - V)_{\rm mean}]^2 + \sum_{k=1}^{N} \left[\frac{\delta(\lambda - V)_k}{N}\right]^2}, \quad (7)$$

where $\sigma(\lambda - V)_{\rm mean}$ is the error of the mean color $\lambda - V$, $\delta(\lambda - V)_k$ is the photometric error of the kth star, and N is the number of stars contained in the corresponding box.

Now, by using this estimate along with the dispersion in both colors and excesses of the reference region, we obtain the uncertainty of the color excess as

$$\Delta(E_{\lambda-V}) = \sqrt{[\Delta(\lambda - V)]^2 + [\sigma(\lambda - V)_{\rm ref}]^2 + [\sigma(E_{\lambda-V})_{\rm ref}]^2}. \quad (8)$$

By means of the uncertainties reported in the last row of Table 1 we obtain $\langle \Delta(E_{B-V}) \rangle = 0.12$, $\langle \Delta(E_{I-V}) \rangle = 0.13$, $\langle \Delta(E_{J-V}) \rangle = 0.18$, $\langle \Delta(E_{H-V}) \rangle = 0.20$, and $\langle \Delta(E_{K-V}) \rangle = 0.22$ for the average uncertainties associated with the different color excess maps.

4. THE RATIO OF TOTAL TO SELECTIVE EXTINCTION

Once the maps of the color excesses have been obtained, they can be used to determine the spatial distribution of R_V across the investigated field. To this end, we exploit different methods which have already been discussed in the literature.

4.1. *Evaluating R_V*

We adopted three methods to obtain the R_V map for CB 107; the first two are based on the characteristics of the extinction curve (CCM; O'Donnell 1994; He et al. 1995; Whittet et al. 2001, 2007; Kandori et al. 2003; Sofia et al. 2005), while the third is based on a minimization technique (He et al. 1995; Gnaciński & Sikorski 1999; Ducati et al. 2003; Geminale & Popowski 2004).

4.1.1. *BVK Method*

This method for obtaining the R_V map is based on the limiting behavior of equation (2) at long wavelengths. In principle, the longer the wavelength the better the approximation, even if, in practice, we must limit ourselves to the near-IR because the dust emission adds to the extinction and begins to be non-negligible at longer wavelengths. Because of this, the K band is generally considered the longest nonthermal wavelength unaffected by dust emission, so that the relationship involving this band reads

$$R_V \simeq 1.1 \frac{E_{V-K}}{E_{B-V}}, \quad (9)$$

TABLE 1
$\lambda - V$ Colors and E_{B-V} Color Excess for Reference Boxes

Box[a]	$B-V$[b]	$V-I$[b]	$V-J$[b]	$V-H$[b]	$V-K$[b]	E_{B-V}[c]
[1, 1]	1.56±0.36	1.97±0.60	3.13±1.03	3.83±1.19	3.84±1.39	0.34±0.24
[2, 1]	1.47±0.42	1.80±0.48	3.03±0.81	3.70±0.95	3.83±1.01	0.32±0.22
[7, 1]	1.43±0.48	1.81±0.46	2.97±0.83	3.59±1.00	3.76±1.07	0.32±0.21
[1, 2]	1.48±0.44	1.84±0.45	3.12±0.78	3.77±0.94	3.85±1.06	0.32±0.20
[1, 5]	1.54±0.45	1.85±0.51	3.07±0.79	3.68±1.01	3.82±1.14	0.37±0.26
[2, 5]	1.55±0.42	1.89±0.48	3.13±0.75	3.77±0.89	3.92±0.95	0.37±0.20
[2, 6]	1.56±0.48	1.93±0.47	3.29±0.84	3.99±0.94	4.12±1.00	0.41±0.23
[1, 7]	1.44±0.56	1.97±0.60	3.28±0.97	3.86±1.23	4.04±1.35	0.43±0.20
[6, 7]	1.56±0.40	1.92±0.45	3.27±0.80	3.91±1.04	4.06±1.12	0.38±0.20
[7, 7]	1.50±0.43	1.82±0.49	3.15±0.76	3.80±0.98	3.98±1.05	0.35±0.25
Mean[d]	1.51±0.05	1.88±0.06	3.14±0.11	3.79±0.12	3.92±0.12	0.36±0.04

[a] Spatial box according to Fig. 2 (*top*).
[b] Mean stellar colors and 1 σ dispersion.
[c] Mean color excess and 1 σ dispersion.
[d] The quoted error is, for each column, the 1 σ dispersion of the mean values.

where the constant is estimated from the standard van de Hulst theoretical curve 15. Because there is a large consensus on the value of this constant (see, e.g., Whittet & van Breda 1978; He et al. 1995; Whittet 2003), we used this relationship as a way to derive the R_V map in our cloud. To this end, we used the photometry obtained in three filters (B, V, and K_s) to estimate the total to selective extinction across CB 107, and then to produce the map R_V (*BVK*) shown in the top left panel of Figure 3.

Note that the effect of a circumstellar shell, significantly contributing to the K-band emission, is to observe a lower K magnitude and then obtain an overestimate for R_V. This is, however, an improbable occurrence because the $J - H$ versus $H - K_s$ diagram in Figure 4 shows that the stars are tightly concentrated in the reddened strip, so that their excesses can be safely attributed to genuine reddening.

It is interesting that the overplotted R_V contour levels (Fig. 3) closely follow the optical shape of the globule, as can be seen in the bottom right panel of the same figure, where they are superimposed on the B-band image of CB 107. This close resemblance allows us to speculate that if the R_V variations are produced by grain growth mechanisms active in this cloud, the timescales involved in changing the optical properties of the dust must be shorter than the dynamical timescales of the cloud itself.

The optical limit of CB 107 clearly shows a value of the R_V contour level similar to the value $R_V = 3.1$ assumed for the reference region which is typical of the interstellar medium. It is also worth noting that the observed increase of R_V toward the innermost regions suggests that the grain size distribution, in this globule, is biased toward larger sizes in regions of higher density, where the grain growth mechanisms can be more efficient.

4.1.2. *Fit Method*

This method is based on equation (6), which is a convenient analytic representation of the extinction curve from the I to the M spectral band (Martin & Whittet 1990; He et al. 1995). In fact, there is observational evidence suggesting that this relationship applies to a variety of lines of sight, from diffuse to dense molecular clouds, with values of the power-law index generally in the range $\beta = 1.6$–2.0 even if, more recently, values as large as $\beta \simeq 2.3$ have been reported in the Coalsack region (Naoi et al. 2007) and along high Galactic latitude lines of sight (Larson & Whittet 2005).

For wavelengths shorter than the I band ($\lambda < 0.9\ \mu$m), the spectral behavior of the extinction significantly changes from one environment to the other (Martin & Whittet 1990) due to variations in the properties of dust grains. However, because in the following we shall adopt the usual normalization of the extinction curve to the E_{B-V} color excess, the normalized excesses will appear in our plots to be differentiated in the long-wavelength tail.

In Figure 5, we present the averaged extinction curve $E_{\lambda-V}/E_{B-V}$ as a function of λ^{-1} (*solid lines*) obtained for some boxes in the CB 107 region, along with the standard extinction curve (*dashed lines*), which is also shown for comparison. Note that, where the sampling box corresponds to the most obscured regions, the extinction curve is quite different from the standard case, pointing out that in the darkest region there is a significant change in the dust properties.

By using the color excess maps we can thus derive the R_V map on the same spatial grid by means of equation (6). In this way, considering the quantities $\lambda^{-\beta}$ and $E_{\lambda-V}/E_{B-V}$ as independent and dependent variables, respectively, we can obtain a linear fit for the extinction curve in each box. Because the power-law index β can be variable (see, e.g., Martin & Whittet 1990; Larson & Whittet 2005; Naoi et al. 2007), we adopted the R_V values previously obtained with the *BVK* method as a starting point to estimate the β exponent, in each box, by fitting equation (6). These values, which are in the range $\beta = 1.86$–2.02, were used in the same equation (6) to derive R_V with the fit method. In this way, the corresponding map (labeled "fit"; Fig. 3, *top right*), was obtained. The reader should, however, consider that by adopting a constant value for β, one can obtain a good, albeit less accurate, approximation to the R_V map.

4.1.3. *CCM Method*

The R_V map can be also obtained with a minimization procedure. If we use the CCM extinction law

$$\frac{A_\lambda}{A_V} = a_\lambda + \frac{b_\lambda}{R_V}, \tag{10}$$

the normalized color excesses at each wavelength can be expressed as

$$\frac{E_{\lambda-V}}{E_{B-V}} = R_V(a_\lambda - 1) + b_\lambda. \tag{11}$$

Thus, for a given box, the total to selective extinction R_V can also be determined by minimizing the sum of the residuals between

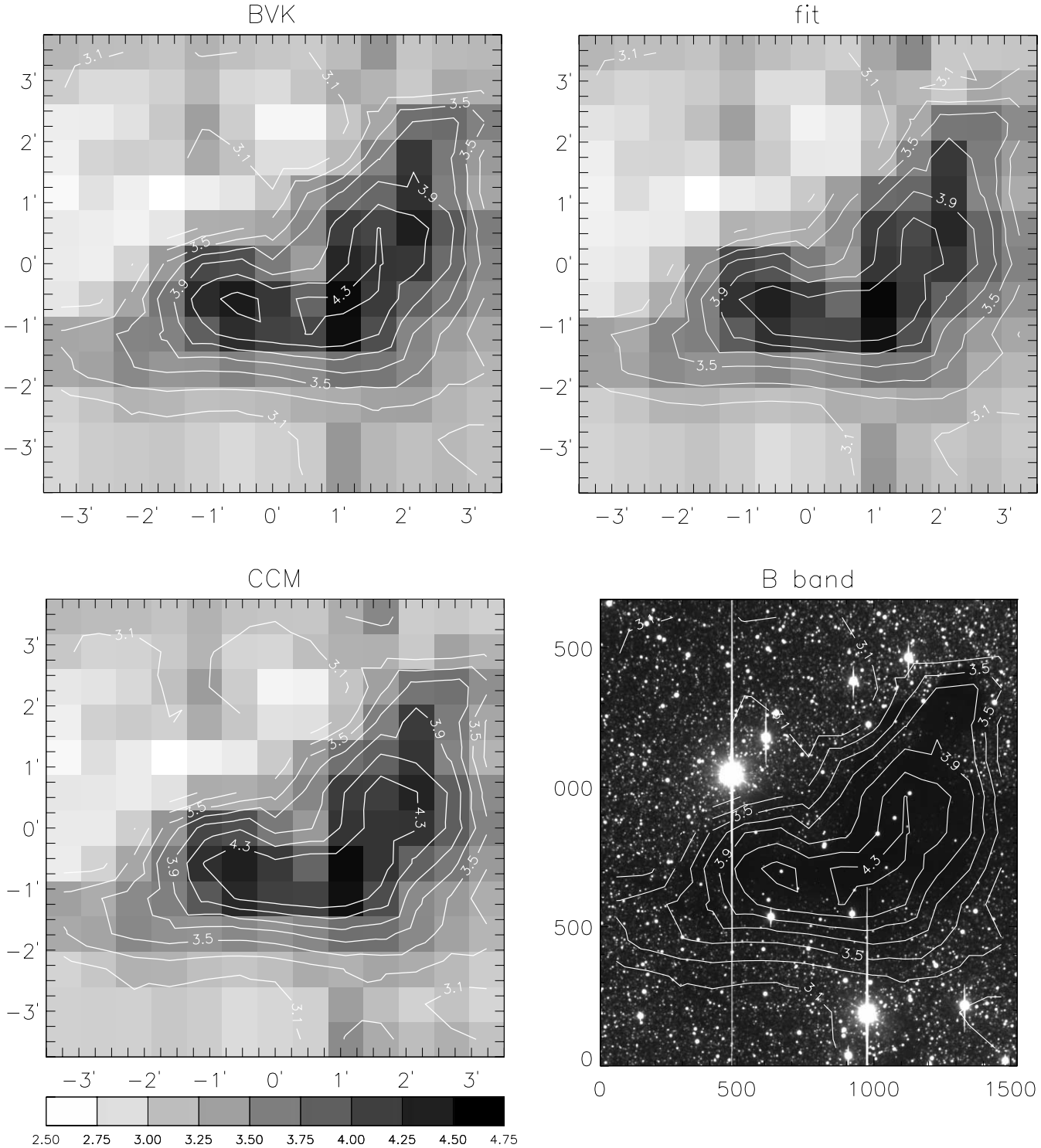

FIG. 3.—R_V maps obtained for CB 107 with the three methods described in the text. *Top left*: $R_V(BVK)$. *Top right*: R_V(fit). *Bottom left*: R_V(CCM). The axes are labeled with the distance, in primes, from the central position whose coordinates are the same as in Fig. 1. The superimposed contour levels, drawn in steps of $\Delta R_V = 0.2$, start from $R_V = 3.1$ and are determined after a 2×2 smoothing of the Nyquist sampled maps. In the bottom right panel, the $R_V(BVK)$ contour levels have been superimposed on the *B*-band image to show the close spatial correspondence with the optical shape of the globule. The axes of the *B* image are in pixels.

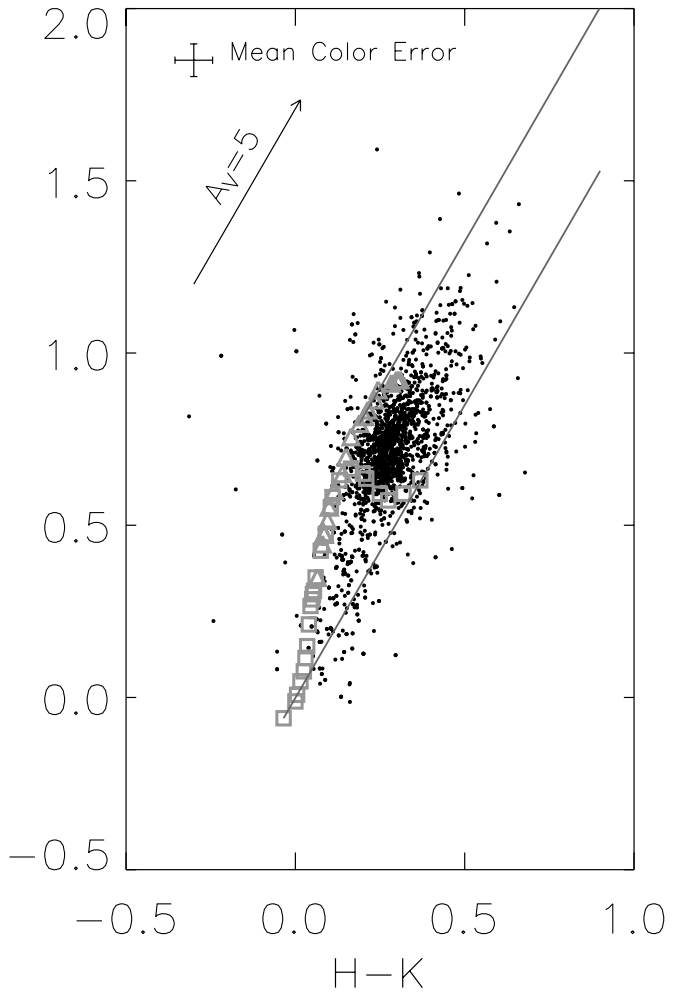

FIG. 4.—$J - H$ vs. $H - K_s$ diagram for the stars detected in both optical and near-IR bands. The locus of the unreddened dwarf and giant stars is also shown, and two parallel continuous lines delimit the region in which the stellar colors are moved by reddening. The mean error is shown in the upper left, along with the reddening vector corresponding to a visual absorption $A_V = 5$ mag.

the observed normalized color excess and the predicted theoretical values (eq. [11]):

$$\chi^2 = \sum_{\lambda} \left[\frac{E_{\lambda - V}}{E_{B-V}} - R_V(a_\lambda - 1) - b_\lambda \right]^2, \tag{12}$$

where the index λ runs over all wavelengths for which we have observational data.

To minimize, we set $d\chi^2/dR_V = 0$ as usual, obtaining

$$R_V = \frac{f_1 - f_2}{f_3}, \tag{13}$$

where the functions f_1, f_2, and f_3 are defined by

$$f_1 = \sum_{\lambda} \frac{E_{\lambda - V}}{E_{B-V}}(a_\lambda - 1), \tag{14}$$

$$f_2 = \sum_{\lambda} b_\lambda (a_\lambda - 1), \tag{15}$$

$$f_3 = \sum_{\lambda} (a_\lambda - 1)^2. \tag{16}$$

Then, by using the previously determined mean color excesses in equation (13), we obtain the R_V (CCM) map shown in the bottom left panel of Figure 3.

4.2. *Uncertainty in R_V Maps*

The uncertainties in color excesses discussed in § 3.1 allow us to estimate those associated with the R_V values obtained with the three methods we used. In the first method, we exploit the approximation given by equation (9) so that, once the uncertainties in the color excesses are known, we evaluate the R_V uncertainty by the usual error propagation. Thus, for each box we have

$$\Delta[R_V(BVK)] = 1.1 \sqrt{\left[\frac{\Delta(E_{V-K})}{E_{B-V}} \right]^2 + \left[\frac{E_{V-K}}{(E_{B-V})^2} \Delta(E_{B-V}) \right]^2}. \tag{17}$$

The second method is based on a fitting procedure (eq. [6]) in which we estimate the uncertainty on the R_V value as the statistical error of the fit. This is computed after adopting, as error associated to each point of the extinction curve, the expression

$$\Delta \left[\frac{E_{\lambda - V}}{E_{B-V}} \right] = \sqrt{\left[\frac{\Delta(E_{\lambda - V})}{E_{B-V}} \right]^2 + \left[\frac{E_{\lambda - V}}{(E_{B-V})^2} \Delta(E_{B-V}) \right]^2}, \tag{18}$$

where the errors in the color excesses refer to each box and are assumed to be uncorrelated.

The uncertainties associated to the third method, which uses equation (13) to determine R_V, have also been estimated by means of error propagation. Considering the values of the constants a_λ and b_λ unaffected by errors and given by the extinction law of CCM, we obtain for each box

$$\Delta[R_V(\mathrm{CCM})] = \frac{\Delta f_1}{f_3}, \tag{19}$$

where Δf_1 is given by

$$\Delta f_1 = \sqrt{\sum_{\lambda} \left\{ (a_\lambda - 1)^2 \Delta \left[\frac{E_{\lambda - V}}{E_{B-V}} \right]^2 \right\}}. \tag{20}$$

In Figure 6 we report, with different symbols, the uncertainties ΔR_V obtained as a function of R_V for the three methods used. As we can see, they increase with R_V in such a way that the *BVK* method gives slightly larger uncertainties compared to the other cases. Note however that, for the CCM and fit methods, the uncertainties are always lower than $\Delta R_V \sim 1$.

It is also worth noting that the values of these uncertainties are in agreement with the results of Larson & Whittet (2005). These authors carefully investigated different sources of uncertainty in R_V showing that, with photometric errors $\delta(m_V) < 0.1$ mag and extinction $A_V \sim 3$ mag, the uncertainty amounts to $\Delta R_V \sim 1$.

4.3. *Comparison of the Methods*

The R_V maps obtained with the three methods discussed and shown in Figure 3 clearly appear very similar, as is also shown by their correlation, on a pixel-by-pixel basis, reported in Figure 7,

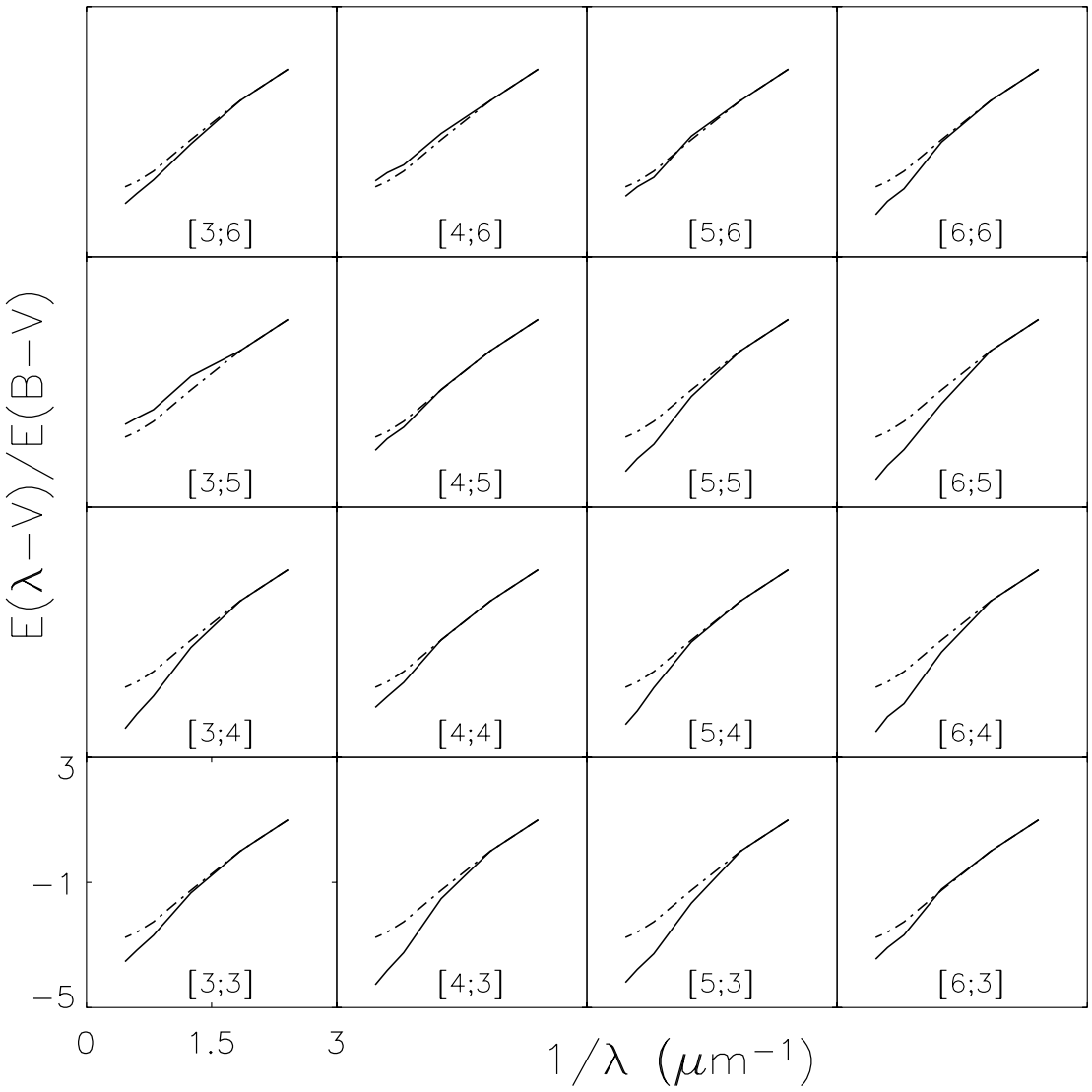

FIG. 5.— Average extinction curves for some grid boxes in the region of CB 107 (see Fig. 2). The axes are labeled only for the lower left box, being the same everywhere. The solid line indicates the mean extinction curve obtained in each box, while the dashed line represents the standard extinction curve.

where the solid lines represent the linear best fit corresponding to the equations

$$R_V(BVK) = (1.05 \pm 0.01) \times R_V(\text{fit}) - (0.10 \pm 0.02),$$
$$R_V(\text{CCM}) = (1.14 \pm 0.01) \times R_V(\text{fit}) - (0.36 \pm 0.01). \quad (21)$$

The tight correlation supports the use of equation (9) on a large range of R_V values, as well as the use of the CCM extinction law for both diffuse and dense IS regions.

Because of this we conclude that, once the color excesses are known, the three methods can be equivalently used to estimate the total to selective extinction, even if, on the basis of the estimated uncertainties shown in Figure 6, either the CCM or the fit method is preferred.

Our use of these three methods is not intended to prove their internal consistency, already investigated in previous literature, but rather as a test for possible differences produced in the final maps by the approximations underlying the different descriptions of the extinction curve.

For completeness, we also mention another procedure of minimization applied by Ducati et al. (2003) to simultaneously determine the values of A_V and R_V by means of multiband $U - N$ photometry. These authors note that the R_V values derived with their method are typically larger than those reported by other investigators (as, e.g., Aiello et al. 1988; He et al. 1995; Vrba & Rydgren 1985; O'Donnell 1994; CCM) for stars in different Galactic directions. These systematics have been explained as an effect of both the different intrinsic colors adopted in their photometric tables and the limited range of applicability, from U to L band, of the CCM extinction law.

For the sake of comparison with the methods adopted here we applied the Ducati et al. (2003) relationships to our data, and discovered that, although the shape of the R_V map is preserved, the pixel values are systematically larger, as we can see in Figure 8, in which the differences typically amount to $\Delta R_V \sim 0.9$. Because in our case the observational data and the photometric system are the same, this discrepancy could be due to the limited spectral coverage of our photometry. In fact, as also pointed out by Ducati et al. (2003), R_V and A_V are better derived using a large range of color excesses, preferably from U to L. The lack of data in the longer wavelengths tends to produce larger R_V, as we have found by using our data, which are limited to the K_s band.

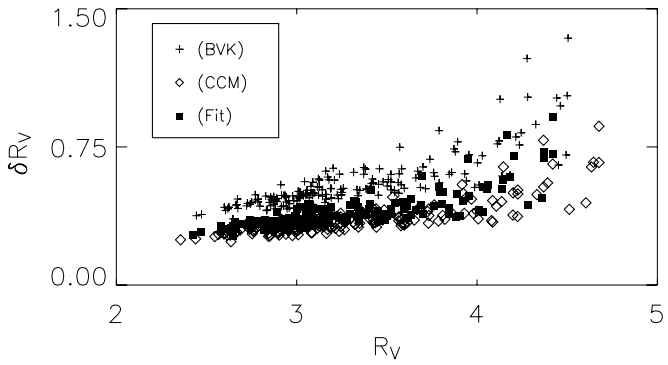

FIG. 6.—Uncertainties ΔR_V as a function of R_V for the three methods discussed in the text. The errors for the CCM and fit methods are always $\Delta R_V < 1$, while they tend to be slightly larger for $R_V \gtrsim 4$ by using the *BVK* method.

4.4. R_V Values Along Single Lines of Sight

The R_V maps shown in Figure 3 were determined by using color excesses evaluated as mean values of the stellar excesses in each grid box. However, the three methods can also be applied to estimate R_V along the lines of sight of individual stars, under the assumption that the mean colors, previously determined in the reference region, can be adopted as intrinsic colors for each star.

Of course we are aware that this approach is far from rigorous, because we replace the true intrinsic stellar color with an average value. We are, however, encouraged in this direction by the profitable use of this approximation made by Arce & Goodman (1999) and Kandori et al. (2003).

We then applied equations (6), (9), and (13) to single stars, obtaining an estimate of R_V on their lines of sight. Note, however, that we only used objects with $E_{B-V} > 0.1$, to avoid large uncertainties due to photometric errors. Subsequently, by sampling the field with the same spatial grid previously used, we obtained the mean R_V on each box and then the R_V maps shown in Figure 9.

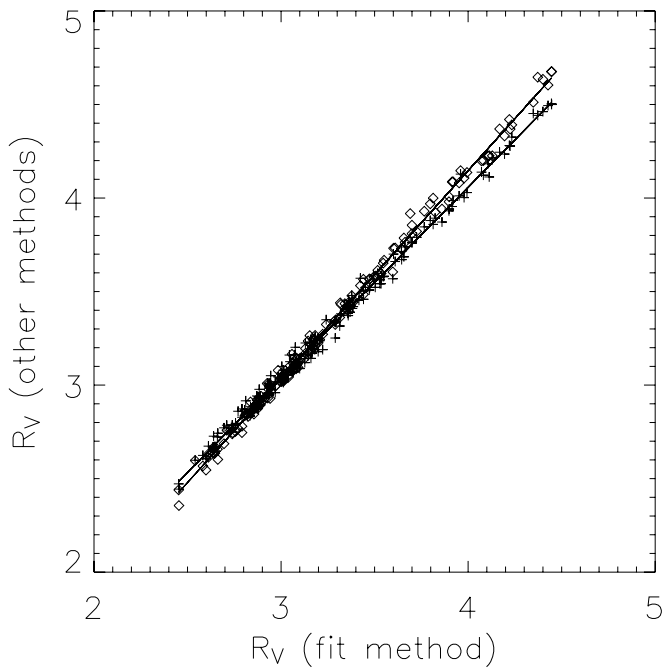

FIG. 7.—R_V map values obtained with the *BVK* (*crosses*) and the CCM (*diamonds*) methods against the corresponding pixel values obtained with the fit method. The straight lines are the corresponding least-squares fit given by eq. (21).

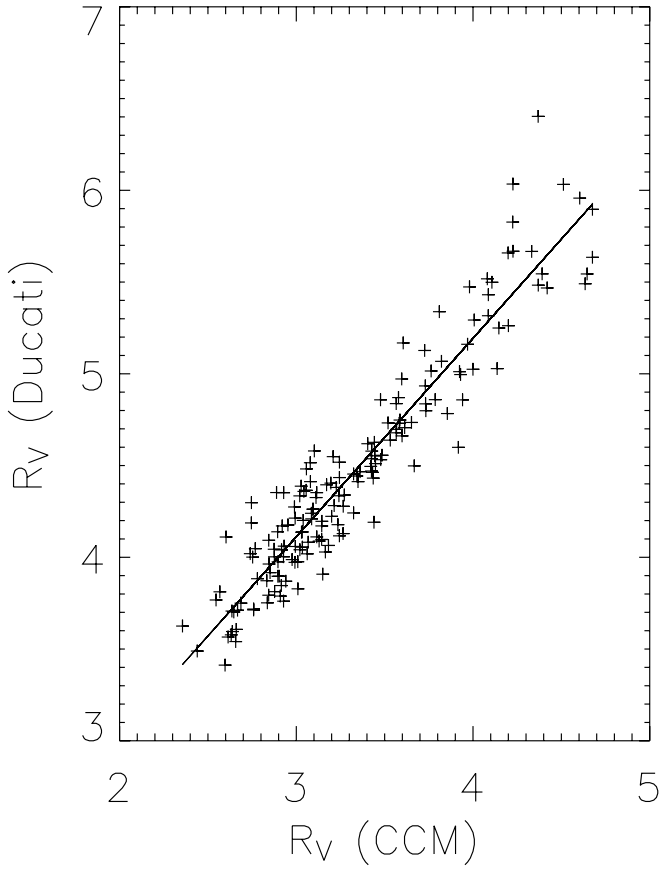

FIG. 8.—Comparison between the R_V values obtained with the Ducati et al. (2003) method and those determined with the CCM method. The least-squares fit (*straight line*) is given by the equation $R_V(\text{Ducati}) = (1.08 \pm 0.03)R_V(\text{CCM}) + (0.87 \pm 0.09)$.

In Figure 10, we present the histogram of both the power law exponent β and the corresponding R_V values as determined, for the background stars, with the fit method. It is evident that the β exponents, obtained along single lines of sight, show a large range of values with a mean $\beta = 1.92$, which is noticeably larger than the CCM value of $\beta = 1.63$, and even greater than the value reported by Whittet (2003), $\beta = 1.84$. These β values are shown in the left panel of Figure 10 and were used to derive the corresponding R_V shown in the right panel. Note that, taking the spatial box average of β along single lines of sight, we recover the range of values reported in § 4.1.2.

The distribution of the R_V appears clearly asymmetric around its peak at $R_V \simeq 3$, as we expect for a molecular cloud in which the environmental conditions are such that the mean size of dust grains increases, producing in turn an increase of the R_V value. For comparison, we also draw the histogram (*dashed line*) obtained for lines of sight crossing the diffuse IS medium by He et al. (1995), normalized to our peak value to show more clearly the conspicuous tail toward the large R_V values.

Another way to highlight the fact that the properties of the dust grains, which affect the value of the R_V parameter, are changing in CB 107 is given in Figure 11, where we plot the E_{B-V} versus E_{V-K} diagram for the background stars. According to equation (9), if R_V is constant, the relationship between the two color excesses is expected to be a simple straight line through the origin, whose slope is $1.1/R_V$. The distribution of the points in the scatter plot clearly shows that they are not aligned along a straight line, particularly those with $E_{V-K} \gtrsim 3$,

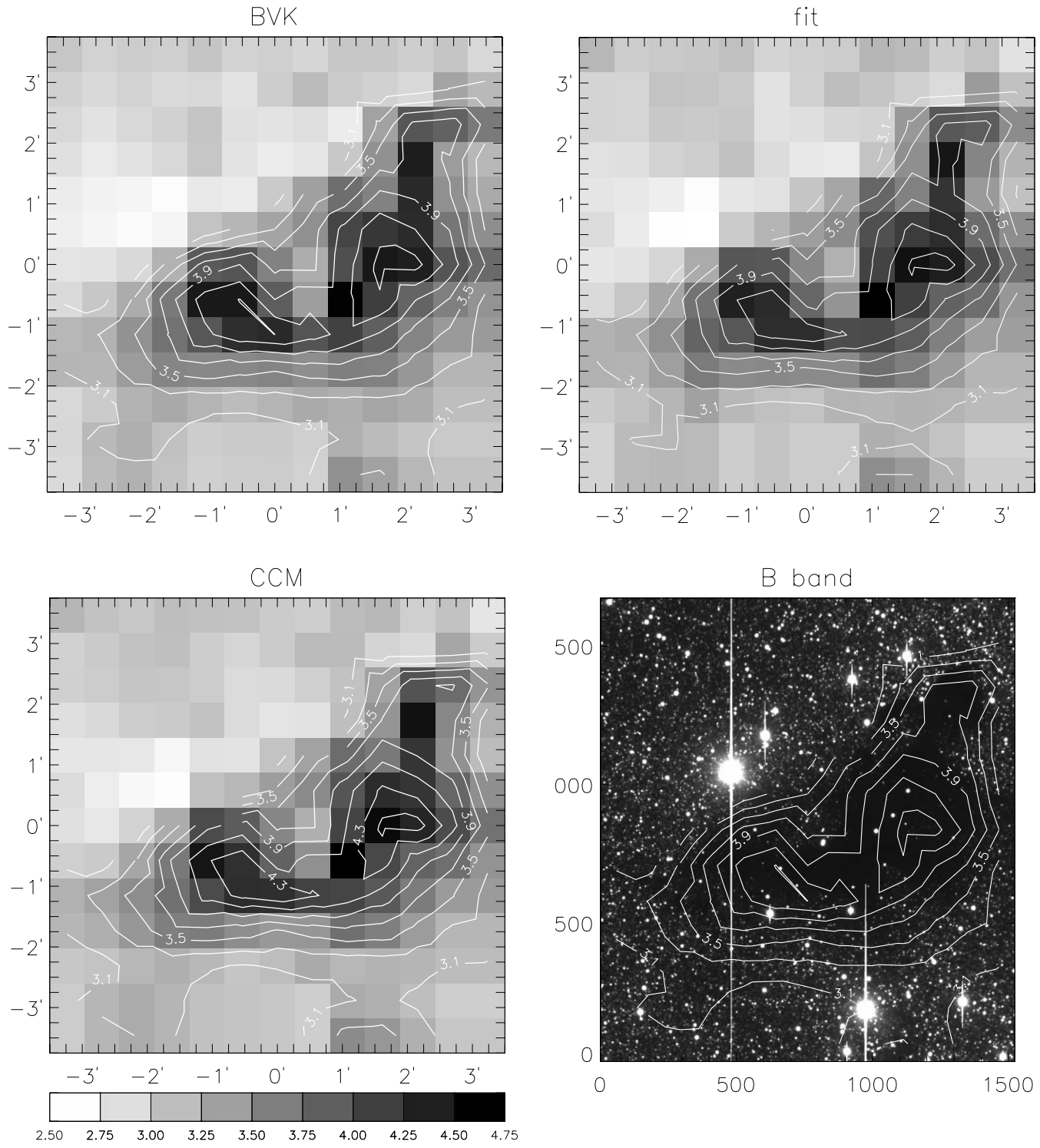

FIG. 9.—R_V maps representing, in each box, the mean of the distribution of the single star values. The contour levels are determined after a 2×2 smoothing and superimposed on each map. The panels sequence, the spatial dimension of the grid box, the labels, and the values of the contours are the same as in Fig. 3.

which correspond to lines of sight crossing the innermost cloud regions.

5. DISCUSSION

An attempt to derive the total to selective extinction map of CB 107 has already been made in a previous paper (Strafella et al. 2001) by using stellar counts to obtain the extinction map in both B and V bands. Taking into account that the field we consider here is limited by the need to overlap the optical and near-IR observations, we note that the lower left corner of the panels in Figure 9 corresponds to the position $x \sim 300$, $y \sim 200$ pixels in the R_V contour map shown in Strafella et al. (2001), Figure 8.

Considering this spatial shift, we see that the maps in Figure 9 are defined in the whole investigated field, while in the previous R_V map only the rightmost part of the globule was defined as a result of the threshold $E_{B-V} > 0.1$ mag, necessary in a box to avoid large uncertainties. Because the three methods we exploit here are more reliable, we shall focus in the following only on these.

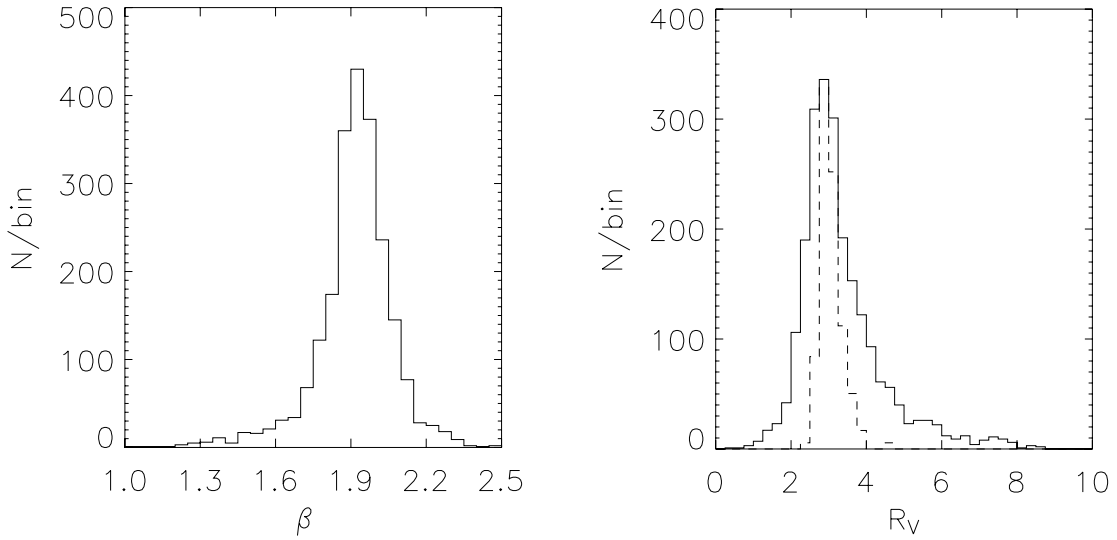

FIG. 10.—*Left*: Histogram of the power-law exponents β as obtained from eq. (6) along the lines of sight of the background stars (see § 4.1.2). *Right*: Histogram of the corresponding R_V, obtained with the fit method. The dashed line represents the histogram obtained by He et al. (1995) scaled to our peak value, for the diffuse IS medium.

Once the R_V values along lines of sight of individual stars were derived, we obtained the maps shown in Figure 9, in which each pixel contains the local information on R_V averaged on a spatial square box of size $L \sim 60''$. Since we also computed the dispersion σ_{R_V} in each pixel, we can now discuss the behavior of the σ_{R_V} versus R_V relation in analogy with previous studies that focused on the extinction.

In this respect, the works of Lada et al. (1994), Alves et al. (1998), Lada et al. (1999), and Campeggio et al. (2004) on dark clouds have shown that the correlation between A_V and its fluctuations σ_{A_V} is now supported by observational evidence. In all the studied cases, the dispersion in the extinction values obtained in a given spatial box has been found to increase with the mean extinction. This behavior has generally been interpreted as evidence for significant column density structure at spatial scales smaller than those defined by the box size used.

In this sense, the characteristics of this relationship can be used as a tool for studying the density fluctuations in the IS clouds at the very small scales probed by the line of sight to a single star. To this end, many theoretical models have been developed to describe IS clouds, some of which consider the clouds as a collection of clumps with different possible characteristics (Lada et al. 1994; Maiolo et al. 2007). On the other hand, Padoan et al. (1997) considered clouds generated as random three-dimensional density distributions with given statistical properties and power spectra. Further possibilities have also been considered by Juvela (1998), who presented different 3D models: a fractal structure, a hierarchy of spherical clumps, and an extreme case in which the cloud volume is filled with cells with either zero or a fixed density value.

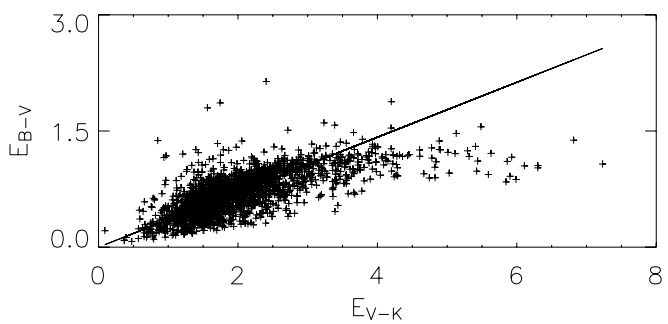

FIG. 11.—Color excesses diagram. The points represent E_{B-V} vs. E_{V-K} determined along single lines of sight. The solid line corresponds to the standard extinction law with $R_V = 3.1$.

In all these simulations, the authors were able to reproduce the main features of the observed σ_{A_V} versus A_V relationship, as well as, for suitable values of the model parameters, the observed values of the slope, which is a parameter that can be related to the internal structure. While these results suggest that the observations are consistent with models of highly structured clouds, they also imply that the slope of this relation cannot, by itself, be used to discriminate among different models. In this respect we recall that the cloud structure is often considered to be the result of an interplay among supersonic turbulent flows and gravitational and magnetic forces, so that it is expected that realistic models, which fully consider the involved physics, should produce quite complex structures. In order to better constrain the models, another tool can be envisaged, which is related to the variations of the slope with the spatial scale investigated (see, e.g., Lada et al. 1999; Campeggio et al. 2004; Maiolo et al. 2007). In analogy with previous studies on extinction, in the following we discuss the relationship σ_{R_V} versus R_V.

5.1. *The σ_{R_V} Versus R_V Relation*

Given the R_V maps shown in Figure 9 and the corresponding dispersion σ_{R_V}, we were able to draw the σ_{R_V} versus R_V scatter plot for CB 107, which is presented in the middle panel of Figure 12. In this figure, two other panels are also shown, corresponding to different choices of the box size. All these scatter plots have been drawn using the estimates of R_V obtained by means of the CCM method (see § 4.4), since the results are equivalent to those of the other methods.

It is remarkable that, similarly to the trend observed for A_V, the dispersion σ_{R_V} systematically increases with R_V, independently of the box size adopted. The understanding of this trend for R_V is clearly more complicated than that for A_V, because one should take into account, in addition to the column density, another variable that plays a role in modeling the cloud, namely the mean grain size, which is thought to be responsible for the variations in R_V. In any case, these results suggest that the mean grain size is a quite variable quantity among different lines of sight, and its

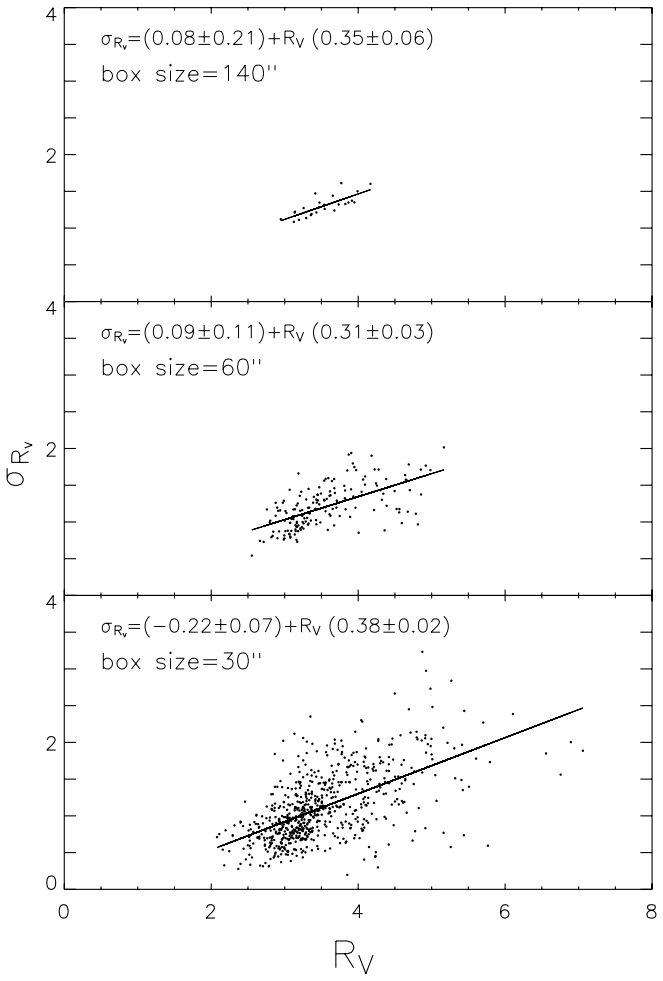

FIG. 12.—σ_{R_V} vs. R_V relation obtained in CB 107 for three different spatial resolutions, as indicated in the panels. The solid lines and the equations reported are the least-squares linear fit to the data points.

fluctuation, quantified by σ_{R_V}, increases in the lines of sight crossing the innermost regions, where the R_V values are larger.

To further investigate the characteristics of the σ_{R_V} versus R_V relation, we extended this analysis to a range of spatial scales, progressively increasing the number of grid boxes covering the CB 107 field. By spatial scanning at the Nyquist frequency, we obtained the plot shown in Figure 13. Note that the largest and

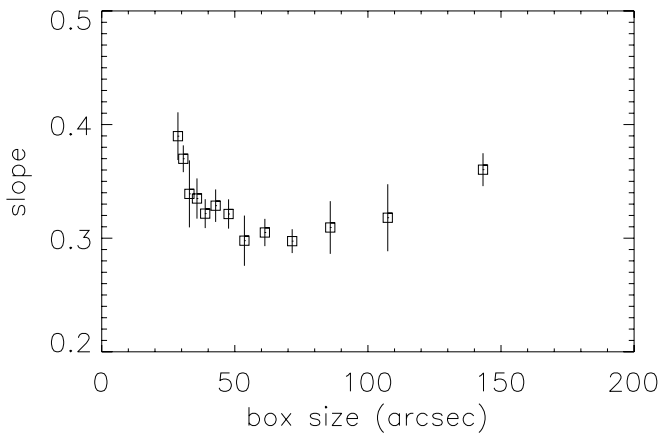

FIG. 13.—Slope of the σ_{R_V} vs. R_V relation as a function of the spatial scale. The errors are 1 σ and have been estimated as described in the text.

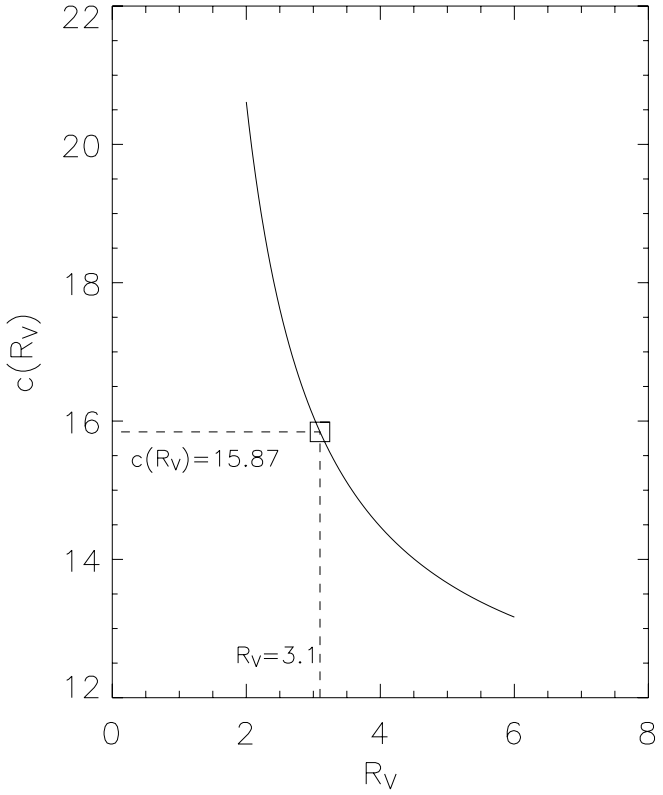

FIG. 14.—Constant of eq. (22) computed as a function of R_V by means of the CCM parameterization of the extinction curve. The square symbol marks the value corresponding to the standard case $R_V = 3.1$.

smallest scale investigated, corresponding to $L \sim 140''$ and $L \sim 30''$, respectively, were chosen to obtain, at the same time, a statistically significant number of points in the σ_{R_V} versus R_V diagram and a reasonable spatial sampling of the dark region.

To estimate the slope uncertainty, we repeated the same procedure while randomly changing the starting point of the scanning grid, obtaining in this way, for each spatial scale, the average value and the dispersion of the σ_{R_V}-R_V slope, which is reported in Figure 13. This figure shows that the slope decreases with the box size until, for sizes $L \gtrsim 80''$, it begins to increase. Note that this trend is quite different from that found for the extinction, where the slope of the σ_{A_V} versus A_V relation systematically increases with the box size (see, e.g., Lada et al. 1999; Campeggio et al. 2004; Maiolo et al. 2007).

Another point we can explore here is the effect of a variable R_V in deriving both the A_V map and the σ_{A_V} versus A_V relation. To this end, we considered the stars falling between the two reddening lines in Figure 4 to evaluate the $H - K_s$ color excess that allowed us to compute the corresponding A_V according to the relation

$$A_V = c(R_V)E_{H-K}, \tag{22}$$

where c is a constant that can be computed once the extinction curve is known. In general it is given by $c = 1/(A_H/A_V - A_K/A_V)$ and, by using the CCM parameterization, its value for the diffuse IS medium is $c(R_V = 3.1) = 15.87$. In our case, we computed this value as a function of R_V, obtaining the result shown in Figure 14 for $2 < R_V < 6$. In this way, exploiting the knowledge of R_V along the lines of sight of the reddened stars, we derived the values of the constant c, and then the extinctions A_V. Note that we also

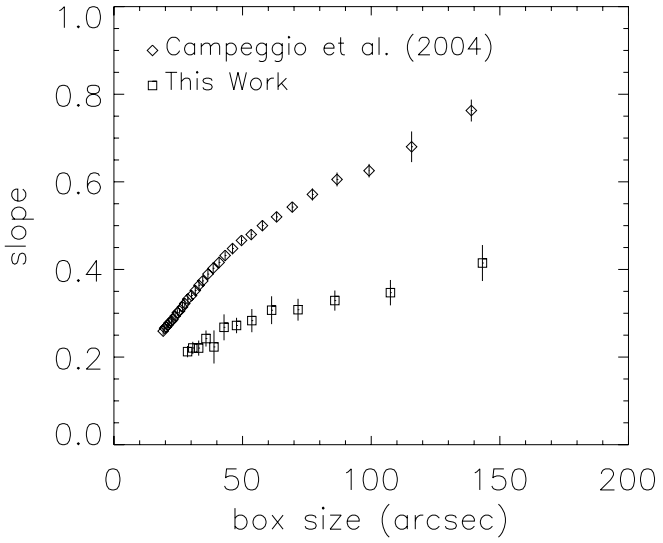

FIG. 15.—Slope of the σ_{A_V} vs. A_V relation reported as a function of the box size used. The lower points are obtained when the effect of a variable R_V is taken into account. The upper points are shown for comparison and refer to a larger sample of background stars, for which the standard value of $R_V = 3.1$ has been assumed (Campeggio et al. 2004). The errors have been estimated as in Fig. 13.

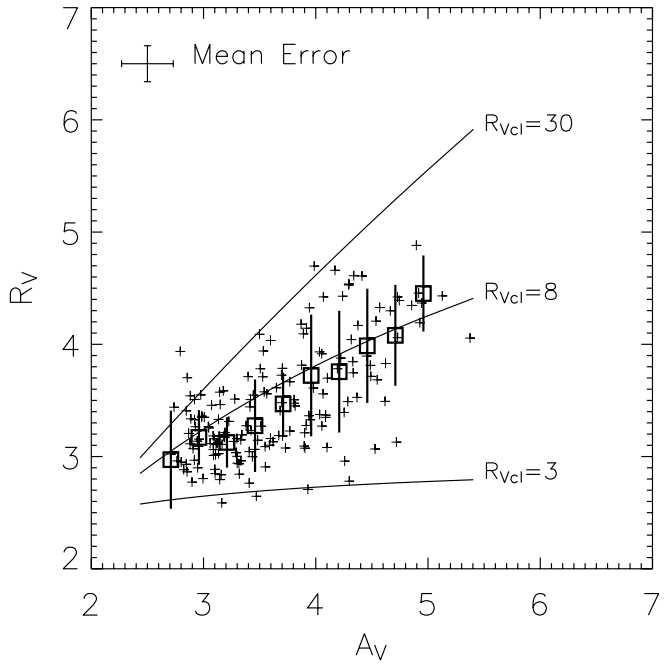

FIG. 16.—Scatter plot of the R_V(fit) vs. A_V values as obtained from the observations. The average uncertainties are shown in the upper left corner. Also shown in bold are the mean R_V and 1 σ dispersions, which have been computed after arranging the A_V in bins of 0.25 mag. The lines represent the relationship between R_V and A_V suggested by the simple model adopted (see text) for three different $R_{V_{cl}}$ values of the model clumps.

verified that the results of this procedure are practically independent of the method we use to obtain R_V.

The A_V values were subsequently used to obtain a scatter plot of σ_{A_V} versus A_V for different spatial scales. The result of this analysis is shown in Figure 15, in which the slope of this relation is plotted as a function of the box size. For comparison, in the same figure, we report the points obtained by Campeggio et al. (2004, Fig. 7), adopting a constant $R_V = 3.1$. These show that, accounting for the variation in R_V, the absolute value of the slope decreases. Note, however, that the stars we use in this work are those detected in both near-IR and optical bands, this sample being the $\sim 12\%$ of those detected in the near-IR and used by Campeggio et al. (2004). As a consequence, the present sample is clearly biased toward the less reddened objects, in particular in the most extinguished regions. On the other hand, using an R_V larger than the standard $R_V = 3.1$ value, we obtained lower mean extinctions and dispersions. Taken together, these two effects can be regarded as responsible for the differences in the plots of Figure 15.

The same considerations help us to understand the differences between the present A_V values and those reported by Campeggio et al. (2004); the extinctions are practically the same at the cloud boundary, while in the innermost regions they are clearly larger in Campeggio et al. (2004). The reason for this is that, by using the full sample of near-IR detected stars, these authors have been able to probe much more extinguished lines of sight, obtaining in this way larger mean extinction values.

5.2. *A Simple Model for CB 107*

The information we obtained on the mean values of R_V is presented in Figure 16 as a function of the box averaged A_V values, which were computed on the same spatial grid. This was done after deriving the single lines of sight extinctions by means of equation (22) while also considering the R_V spatial variations.

It is evident that the trend for A_V is to increase with R_V, as is also shown in Figure 16 by the bold symbols representing the mean R_V values obtained after binning in A_V. This behavior resembles that obtained by Whittet et al. (2001) for the Taurus cloud; therefore, as they did, we adopt here a simple model (see also Whittet 2007) to discuss our observations. Basically, this model considers that CB 107 is made of dense clumps embedded in a more diffuse IS material characterized by $A_V = A_{V_{bg}}$ and $R_V = R_{V_{bg}}$.

Considering the extinction to be produced by two components and using their additivity, we can express the observed value along a line of sight as

$$A_{\lambda_{ob}} = A_{\lambda_{bg}} + \sum_{i=1}^{N} (A_{\lambda_{cl}})_i, \tag{23}$$

where N is the number of clumps intercepted along the investigated direction and the subscripts "ob," "bg," and "cl" refer to observations, background, and clumps respectively. Similarly, for the color E_{B-V}, we can also write

$$E_{(B-V)_{ob}} = E_{(B-V)_{bg}} + \sum_{i=1}^{N} [E_{(B-V)_{cl}}]_i, \tag{24}$$

and, taking into account that $R_V = A_V/E_{B-V}$ by definition, the previous relation becomes

$$R_{V_{ob}} = \frac{A_{V_{ob}}}{A_{V_{bg}}/R_{V_{bg}} + \sum_{i=1}^{N} (A_{V_{cl}})_i/(R_{V_{cl}})_i}. \tag{25}$$

The behavior observed for both the extinction dispersion σ_{A_V} versus A_V and the total to selective extinction dispersion σ_{R_V} versus R_V can be understood if nearby lines of sight intercept a different number of clumps characterized by a different grain size distribution. If this is the case, the use of equation (25) can give us information on $R_{V_{cl}}$ along individual lines of sight. As a further

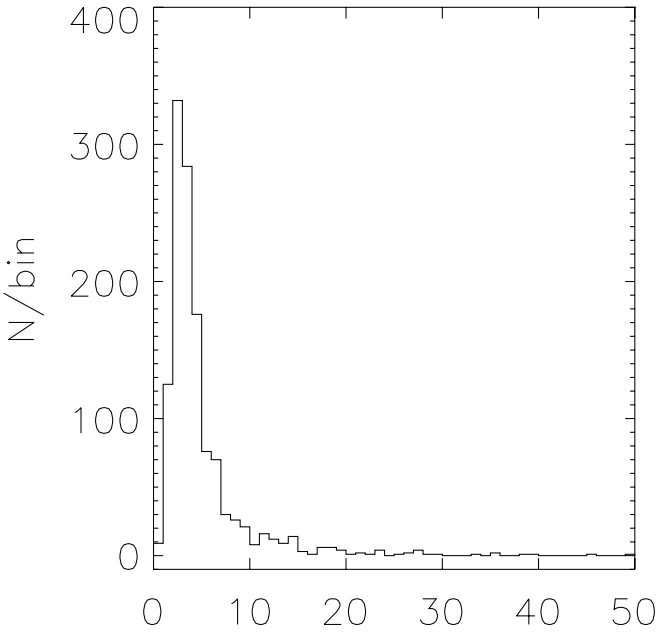

FIG. 17.—Histogram of the $R_{V_{cl}}$ values obtained by means of eq. (26). The bins correspond to $\Delta R_{V_{cl}} = 1$. The x-axis has been downshifted at $y = -10$ to better appreciate the histogram tail.

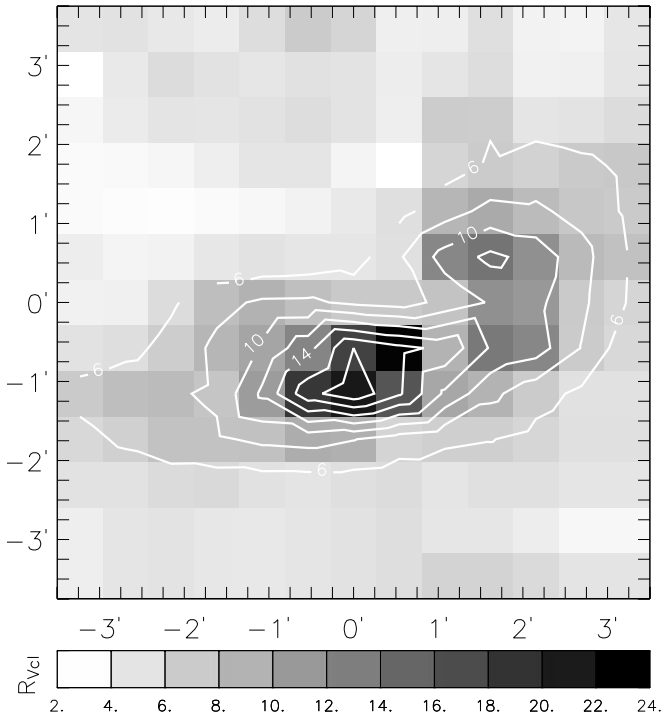

FIG. 18.—$R_{V_{cl}}$ map. The contour levels, which are superimposed, have been drawn in steps of $\Delta R_{V_{cl}} = 2$, starting with $R_{V_{cl}} = 6$, after a 2×2 smoothing. The grid box is the same as in Fig. 9.

simplification of the model, we assume either that each line of sight intercepts a single clump, or that the intercepted clumps are characterized by an average $R_{V_{cl}}$ value. With this assumption, equation (25) can be rewritten as

$$R_{V_{ob}} = \frac{A_{V_{ob}}}{A_{V_{bg}}/R_{V_{bg}} + \left(A_{V_{ob}} - A_{V_{bg}}\right)/R_{V_{cl}}}. \qquad (26)$$

Now, to choose appropriate values for the parameters characterizing the diffuse material in which the clumps are embedded, we adopted values which are representative of the regions outside the globule, namely $A_{V_{bg}} = 2.0$ mag and $R_{V_{bg}} = 2.5$. In this respect, we note that Whittet et al. (2001), when studying the Taurus dark cloud, used different values because in their case R_V is observed to be constant for $A_V < 3.2$ and increasing for larger values. Since this threshold in Taurus is similar to that for the detectability of the H_2O ice absorption feature, these authors argued that the observed increase in R_V is related to the survival of an ice mantle on the dust grains.

In our case, plotting R_V versus A_V as in Figure 16, we find that, on average, R_V increases with A_V in the whole observed extinction range. This suggests that in CB 107, the growth of the grain size, implied by the increase in R_V, could be due to coagulation mechanisms more than to the condensation of ice mantles, a process generally requiring a larger extinction threshold (Whittet et al. 2001 and references quoted therein).

In the same Figure 16, we also plot three curves (*solid lines*) which are representative of the R_V versus A_V relation in equation (26) for different values of the clump parameter $R_{V_{cl}}$. Note that most of the observational points fall between the two curves corresponding to $R_{V_{cl}} = 3$ and $R_{V_{cl}} = 30$, and that the curves converge to the adopted values $R_{V_{bg}} = 2.5$ and $A_{V_{bg}} = 2.0$ mag.

To further investigate the clump properties in CB 107 with this model , we used equation (26) for each line of sight, obtaining the corresponding values for $R_{V_{cl}}$, which are reported in Figure 17 as a histogram. The peak of the distribution falls at $2 < R_{V_{cl}} < 3$, with a pronounced tail toward larger values, including a few cases

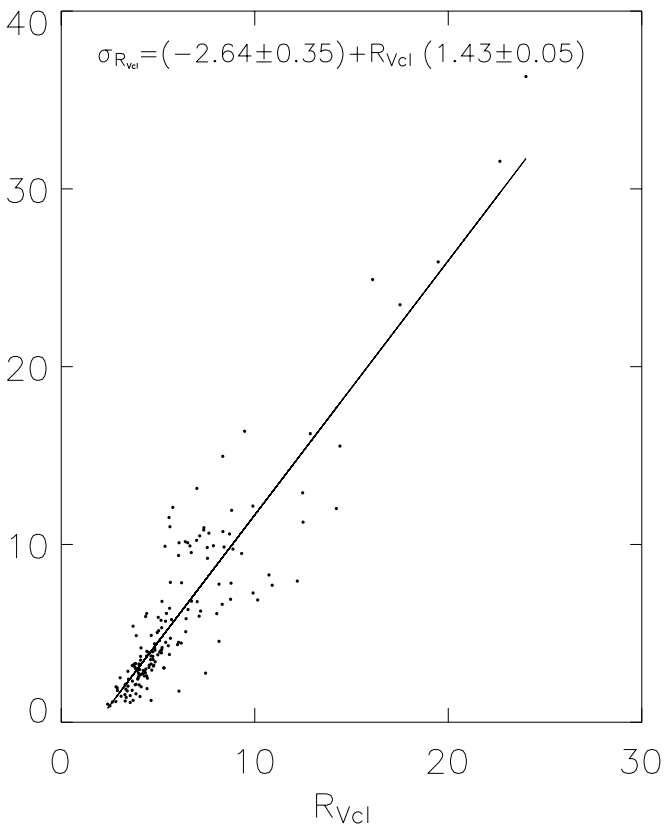

FIG. 19.—$\sigma_{R_{V_{cl}}}$ vs. $R_{V_{cl}}$ relation obtained by using eq. (26). The line represents the least-squares linear fit to the data points. The corresponding equation is shown in the upper part of the figure.

with extremely large values, which are implied by the model to obtain the observed A_V and R_V.

The model results obtained in this way along different lines of sight can be also arranged as a map of the $R_{V_{\rm cl}}$. Adopting the same box size of $L \sim 60''$ and computing spatial averages, we derived the map shown in Figure 18 that is reminiscent of the $R_{V_{\rm ob}}$ map, even if the pixel values are systematically larger than those actually observed. This is particularly true in the innermost dark regions of CB 107, which supports the idea that the grain growth process, which is responsible for the increase in the R_V value, is expected to be more efficiently activated in regions of higher density. However, we point out that the peak values derived for the model clumps are not always spatially coincident with those of the observed maps in Figure 9, suggesting that the relative contribution to the observed R_V of both model clumps and background medium changes with the line of sight.

For each spatial box, in addition to the mean value of $R_{V_{\rm cl}}$, we also determined the dispersion $\sigma_{R_{V_{\rm cl}}}$ that was used to obtain Figure 19. This shows that, in analogy with Figure 12, the dispersion $\sigma_{R_{V_{\rm cl}}}$ increases systematically with $R_{V_{\rm cl}}$ but with a significantly steeper slope. This result suggests that the fluctuation of the dust grain size, required by this model for clumps intercepted by nearby lines of sight, is particularly large in the innermost regions characterized by large values of $R_{V_{\rm cl}}$.

As a final remark we recall that these results were obtained under the hypothesis that the clumps intercepted by a given line of sight are characterized by the same R_V, an assumption that clearly represents a limit for the model.

6. SUMMARY AND CONCLUSIONS

We used imaging in the optical and near-IR photometric bands to obtain the R_V distribution across the dark cloud CB 107. To do this, we derived color excess maps under the assumption that the mean intrinsic stellar colors $\lambda - V$ in the investigated field are well represented by the mean stellar colors in a reference region. The R_V maps were then obtained with three different methods:

1. Using the relationship among the color excesses E_{B-V} and E_{V-K} (*BVK* method).
2. Extinction curve fitting (fit method).
3. A minimization procedure involving the CCM extinction law (CCM method).

The maps suggest that in this cloud, the mean size of the dust grain component is noticeably larger than in the diffuse IS medium.

After the analysis of the estimated uncertainties associated with the R_V values, we conclude that the three methods can be equivalently used, even though the fit and the CCM methods might be preferred due to the slightly lower uncertainties involved.

The R_V values on single lines of sight were obtained by adopting the mean colors of the reference region as representative of the unreddened colors for each star. With this simplification, we estimated the stellar color excesses and then the corresponding R_V values along single lines of sight obtaining, for a given spatial box, the R_V mean value and dispersion. A plot of these quantities has shown that the dispersion σ_{R_V} systematically increases with R_V, a trend similar to that observed for the extinction A_V.

We also discussed the R_V versus A_V relationship in the framework of a simple model as suggested by Whittet et al. (2001). With this model, assuming that CB 107 consists of discrete clumps embedded in a more diffuse IS material, we inferred the clumps parameter $R_{V_{\rm cl}}$, whose values were used to draw the corresponding map. These values are always larger than the observed ones, suggesting that they should be regarded as a lower limit to the values actually characterizing the clumps. This implies that, in the darkest regions of the IS clouds, the mean grain size in the clumps is larger than that derived by simple consideration of the observed R_V values.

We also found that the mean trend of the R_V versus A_V relationship appears to be increasing in the whole range of the observed values, suggesting that the grain growth mechanism in CB 107 is more probably due to coagulation processes than to the condensation of an ice mantle.

Finally, we presented for the first time the observed relationship σ_{R_V} versus R_V, which could be a potential tool to discriminate among different cloud models better than the analogous relation σ_{A_V} versus A_V.

We are grateful to the ESO staff at La Silla for valuable help during the observations. We thank an anonymous referee for helpful suggestions. This work is partly supported by the Italian Ministry for Scientific Research through a PRIN project.

REFERENCES

Aiello, S., Barsella, B., Chlewicki, G., Greenberg, J. M., Patriarchi, P., & Perinotto, M. 1988, A&AS, 73, 195
Alves, J., Lada, C. J., Lada, E. A., Kenyon, S. J., & Phelps, R. 1998, ApJ, 506, 292
Arce, H. G., & Goodman, A. A. 1999, ApJ, 517, 264
Balázs, L. G., Ábrahám, P., Kun, M., Kelemen, J., & Tóth, L. V. 2004, A&A, 425, 133
Cambrésy, L. 1999, A&A, 345, 965
Campeggio, L., Strafella, F., Elia, D., Maiolo, B., Cecchi-Pestellini, C., Aiello, S., & Pezzuto, S. 2004, ApJ, 616, 319
Cardelli, J. A., Clayton, G. C., & Mathis, J. S. 1989, ApJ, 345, 245 (CCM)
Ducati, J. R., Ribeiro, D., & Rembold, S. B. 2003, ApJ, 588, 344
Geminale, A., & Popowski, P. 2004, Acta Astron., 54, 375
Gnaciński, P., & Sikorski, J. 1999, Acta Astron., 49, 577
He, L., Whittet, D. C. B., Kilkenny, D., & Spencer Jones, J. H. 1995, ApJS, 101, 335
Juvela, M. 1998, A&A, 338, 723
Kandori, R., Dobashi, K., Uehara, H., Sato, F., & Yanagisawa, K. 2003, AJ, 126, 1888
Lada, C. J., Alves, J., & Lada, E. A. 1999, ApJ, 512, 250
Lada, C. J., Lada, E. A., Clemens, D. P., & Bally, J. 1994, ApJ, 429, 694
Landolt, A. U. 1992, AJ, 104, 340
Larson, K. A., & Whittet, D. C. B. 2005, ApJ, 623, 897
Launhardt, R., & Henning, T. 1997, A&A, 326, 329
Lombardi, M., & Alves, J. 2001, A&A, 377, 1023
Maiolo, B., Strafella, F., Campeggio, L., Elia, D., & Aiello, S. 2007, ApJ, 661, 926
Martin, P. G., & Whittet, D. C. B. 1990, ApJ, 357, 113
Mathis, J. S. 1990, ARA&A, 28, 37
Naoi, T., et al. 2007, ApJ, 658, 1114
O'Donnell, J. E. 1994, ApJ, 422, 158
Padoan, P., Jones, B. J. T., & Nordlund, A. P. 1997, ApJ, 474, 730
Persson, S. E., Murphy, D. C., Krzeminski, W., Roth, M., & Rieke, M. J. 1998, AJ, 116, 2475
Rieke, G. H., & Lebofsky, M. J. 1985, ApJ, 288, 618
Sofia, U. J., et al. 2005, ApJ, 625, 167
Stetson, P. B. 1987, PASP, 99, 191
Strafella, F., Campeggio, L., Aiello, S., Cecchi-Pestellini, C., & Pezzuto, S. 2001, ApJ, 558, 717
Szomoru, A., & Guhathakurta, P. 1999, AJ, 117, 2226
Valdes, F. G., Campusano, L. E., Velasquez, J. D., & Stetson, P. B. 1995, PASP, 107, 1119
Vrba, F. J., Coyne, G. V., & Tapia, S. 1981, ApJ, 243, 489
Vrba, F. J., & Rydgren, A. E. 1985, AJ, 90, 1490
Whittet, D. C. B. 2003, Dust in the Galactic Environment (2nd ed.; Bristol: IOP)
———. 2007, AJ, 133, 622
Whittet, D. C. B, Gerakines, P. A., Hough, J. H., & Shenoy, S. S. 2001, ApJ, 547, 872
Whittet, D. C. B, & van Breda, I. G. 1978, A&A, 66, 57
———. 1980, MNRAS, 192, 467